Simultaneous Release of Fe and As during the Reductive Dissolution of Pb–As Jarosite by Shewanella putrefaciens CN32

ARTICLE *in* ENVIRONMENTAL SCIENCE & TECHNOLOGY · NOVEMBER 2012

Impact Factor: 5.33 · DOI: 10.1021/es3021809 · Source: PubMed

Environmental Science & Technology

Article

pubs.acs.org/est

Simultaneous Release of Fe and As during the Reductive Dissolution of Pb–As Jarosite by *Shewanella putrefaciens* CN32

Christina M. Smeaton,*[,†,‡,○] Gillian E. Walshe,[†,#] Adrian M. L. Smith,[§,∥,⊥] Karen A. Hudson-Edwards,[⊥] William E. Dubbin,[§] Kate Wright,[∥,¶] Andrew M. Beale,[∥,▼] Brian J. Fryer,[†] and Christopher G. Weisener[†]

[†]Great Lakes Institute for Environmental Research, University of Windsor, Windsor, Ontario N9B 3P4, Canada

[‡]Ecohydrology Research Group, Department of Earth and Environmental Sciences, University of Waterloo, Waterloo, Ontario N2L 3G1, Canada

[§]Department of Mineralogy, The Natural History Museum, Cromwell Road, London, SW7 5BD, U.K.

[∥]Davy Faraday Research Laboratory, The Royal Institution of Great Britain, 21 Albemarle Street, London, W1S 4BS, U.K.

[⊥]Department of Earth and Planetary Sciences, Birkbeck, University of London, Malet Street, London, WC1E 7HX, U.K.

Supporting Information

ABSTRACT: Jarosites are produced during metallurgical processing, on oxidized sulfide deposits, and in acid mine drainage environments. Despite the environmental relevance of jarosites, few studies have examined their biogeochemical stability. This study demonstrates the simultaneous reduction of structural Fe(III) and aqueous As(V) during the dissolution of synthetic Pb–As jarosite ($PbFe_3(SO_4,AsO_4)_2(OH)_6$) by *Shewanella putrefaciens* using batch experiments under anaerobic circumneutral conditions. Fe(III) reduction occurred immediately in inoculated samples while As(V) reduction was observed after 72 h. XANES spectra showed As(III) (14.7%) in the solid phase at 168 h coincident with decreased aqueous As(V). At 336 h, XANES spectra and aqueous speciation analysis demonstrated 20.2% and 3.0% of total As was present as As(III) in the solid and aqueous phase, respectively. In contrast, 12.4% of total Fe was present as aqueous Fe(II) and was below the detection limits of XANES in the solid phase. TEM-EDS analysis at 336 h showed secondary precipitates enriched in Fe and O with minor amounts of As and Pb. Based on experimental data and thermodynamic modeling, we suggest that structural Fe(III) reduction was thermodynamically driven while aqueous As(V) reduction was triggered by detoxification induced to offset the high As(V) (328 μM) concentrations released during dissolution.

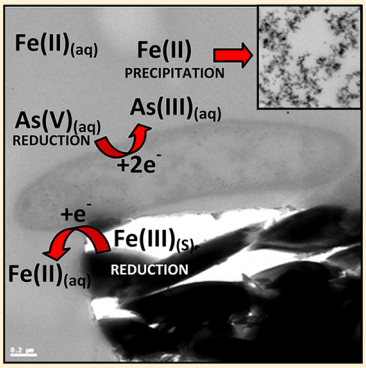

INTRODUCTION

Elevated concentrations of arsenic (As) in groundwater aquifers continue to threaten the health of millions of people worldwide.[1] Redox potential and pH are the most important factors controlling As speciation and under circumneutral oxidizing conditions below pH 6.8, diprotonated arsenate $H_2AsO_4^-$ dominates while monoprotonated $HAsO_4^{2-}$ becomes dominant above pH 6.8. Under reducing conditions below pH 9.2, the uncharged arsenite species H_3AsO_3 is predominant. Arsenite is more toxic than arsenate and reversibly combines with thiol groups to disrupt cellular processes, while arsenate mimics phosphate and enters the cell via transporters meant for PO_4^{3-} and interferes with phosphate based energy-generating processes.[2] Microorganisms mediate As cycling through redox processes and reduce As(V) to As(III) during either detoxification (*ars* system) (As >100 μM) or respiration (*arr* system) (As >100 nM).[2] As(V) is commonly associated with iron (Fe) minerals in sediments through adsorption or coprecipitation onto Fe(III) hydroxide (HFO) surfaces, and the reductive dissolution of these minerals is considered the primary pathway of As solubilization in most surface and subsurface environments.[3−5] As(V) is also incorporated into secondary As minerals such as scorodite ($FeAsO_4{\cdot}2H_2O$), jarosite ($KFe_3(SO_4)_2(OH)_6$), and Pb–As jarosite (i.e., beaudantite, $PbFe_3(SO_4,AsO_4)_2(OH)_6$) through the oxidation of As sulfide minerals such as arsenopyrite (FeAsS) during metallurgical processing, natural weathering, and/or acid mine drainage.

The structure of As substituted minerals is extensively studied, yet As release during dissolution from jarosite-group minerals is less investigated.[6−11] Jarosite-group minerals have the general formula $AB_3(TO_4)_2(OH)_6$, where the A site is occupied by monovalent or divalent cations (e.g., K or Pb), the B site is occupied by cations with octahedral (O) coordination (e.g., Fe(III) or Al(III)), and the T sites correspond to tetrahedral coordination (T) (e.g., S(IV) and As(V)).[12,13] Jarosites typically form under oxidizing, ferric and sulfate rich, and acidic (pH < 3.5) conditions and at pH > 3.5 will dissolve to form goethite or meta stable phases such as schwertmannite

Received: May 31, 2012
Revised: October 24, 2012
Accepted: November 5, 2012
Published: November 5, 2012

or ferrihydrite.[13−15] Jarosite precipitation is also widely utilized in the Zn industry to remove impurities such as Fe, sulfate, alkalis, and other heavy metals (e.g., Pb, Tl, and As) from processing solutions.[16]

Consequently, large volumes of jarosites are produced per year and typically stored in disposal ponds under circumneutral conditions, thereby resulting in dissolution/reprecipitation reactions that may potentially release toxic metals into disposal environments. For example, codisposal of natrojarosite, $NaFe_3(OH)_3(SO_4)_2$, and base-metal sulfide tailings at Kidd Creek, Timmons, Canada (pH 6.5−6.8, Eh = 94−117 mV) caused increased concentrations of Zn, Pb, and As in pore waters associated with the jarosite disposal zone of the tailings pile attributed to enhanced dissolution of jarosites.[17] However, the relative environmental stability of synthetic jarosites over other potential waste mineral hosts such as apatites and pyrochlores has recently made jarosite-type precipitates a potential candidate for long-term disposal of toxic metals such as As, Pb, Bi, Hg, Tl, Sb, Cr, Se, and radioactive isotopes of K, Sr, Th, U, and REE.[18,19] Therefore, determining the biogeochemical stability of jarosites is important to evaluate the potential mobility of metals such as As and Pb from disposal sites. To date, research has demonstrated microbial Fe and S reduction in various jarosites including K jarosite, Pb jarosite, and Ag jarosite, yet the biogeochemical stability of jarosites as it relates to As reduction remains to be elucidated.[20−22] Theoretically, Fe(III) and As(V) reduction are expected to occur at similar redox potentials but the reduction sequence may vary and will also depend on the crystallinity of the Fe(III) phase.[23] For example, incubations of Bengal Delta sediments with native microbial consortia showed Fe(III) reduction prior to As(V) reduction.[3] In contrast, incubations of As(V) adsorbed onto the surface of hydrous ferric oxides with a native microbial consortia or *Shewanella* sp. ANA-3 demonstrated As(V) reduction simultaneously or prior to Fe(III) reduction.[24] While kinetic factors may drive the reduction of As(V) and Fe(III), ultimately thermodynamic favorability will control whether the reaction will proceed through respiration (*arr* system).[25]

This study addresses the relative order and extent of microbial As(V) and Fe(III) reduction in a synthetic Pb−As jarosite by *Shewanella putrefaciens* CN32 using batch experiments under circumneutral anaerobic conditions. *S. putrefaciens* was used because it is a well characterized dissimilatory metal reducing bacteria capable of both As(V) and Fe(III) reduction.[4,25−29] Moreover, to the best of our knowledge, this is the first study to examine the thermodynamic constraints governing the reductive dissolution of jarosites. Additionally, we examine the fate of As and Pb released during both the abiotic and reductive dissolution of Pb−As jarosite.

MATERIALS AND METHODS

Preparation of Pb−As Jarosite/Cell Suspensions and Sampling Protocol. Smith et al. previously reported the synthesis, characterization, and abiotic dissolution of the Pb−As jarosite sample, $(H_3O)_{0.68}Pb_{0.32}Fe_{2.86}(SO_4)_{1.69}(AsO_4)_{0.31}(OH)_{5.59}(H_2O)_{0.41}$, used in this study.[7] To confirm structural As incorporation into the jarosite phase during synthesis, speciation and bonding environments of Fe and As in the original unreacted Pb−As-jarosite sample were determined by EXAFS analysis carried out at the CLRC Synchrotron Radiation Source at Daresbury Laboratory, UK (Supporting Information (SI) Section S4). Pure cultures of *Shewanella putrefaciens* CN 32 cultures (ATC BAA-453) were grown, harvested, and inoculated into a modified M1 minimal media (see SI Section 1 for more details). The minimal media contained the following: 1.34 mM potassium chloride (KCl), 28 mM ammonium chloride (NH_4Cl), 0.68 mM calcium chloride ($CaCl_2$), 50 mM sodium perchlorate ($NaClO_4$), 24 mM Na-lactate (60% syrup), and 20 mM PIPES (1,4-piperazine diethanesulfonic acid) buffer at pH 7.4. All minimal media were transferred to an anaerobic chamber (95% N_2/5% H_2) and 15 mL of the cell suspension was dispensed into 20-mL polypropylene test tubes containing 0.0498 ± 0.0013 g of Pb−As jarosite (21 samples). All samples were capped, sealed with parafilm, covered, and rotated end-over-end at 20 rpm in the anaerobic chamber using a benchtop rotator (Glas Col) at 27 °C and sacrificed in triplicate at 0, 12, 24, 48, 72, 168, and 336 h. Experimental Pb−As jarosite controls contained 15 mL of sterile minimal media and 0.0498 ± 0.0011 g of the jarosite phase in 20-mL polypropylene tubes (21 samples). An additional set of control samples containing 15 mL of the minimal media/cell suspension (i.e., no Pb−As jarosite) were prepared to examine background pH, Eh, cell viability, and elemental concentrations over time (21 samples).

At each sampling period, pH (Thermo Ross Sure-flow semi micro pH probe) and Eh (Thermo Ross Sure Flow combo redox/ORP) were measured in each sample. *S. putrefaciens* metabolism was monitored immediately using the Promega BacTiter-Glo Microbial Cell Viability Assay, an ATP-based luminescent technique (SI Section 2). Starting ATP concentrations were converted to cell counts using an average ATP-per-biovolume concentration of 2.95×10^{-9} nmol/cell ATP and the starting cell concentration was 1.3×10^8 cells/mL.[30]

Solid Phase Characterization. Sample slurries were collected and imaged under low vacuum at a low accelerating voltage (5−10 kv) using field emission−environmental scanning electron microscopy (FE-ESEM, FEI-Quanta 200F). Additional sample slurries (1.0 mL) were collected and preserved in 2.5% gluteraldehyde and stored at 4 °C for transmission electron microscopy (TEM) preparation and analysis (FEI Titan 80-300) (SI Section S3). Solid phase samples for X-ray absorption spectroscopy (XAS) and X-ray diffraction (XRD) analysis were collected via filtration onto nylon 0.45-μm filter paper (Whatman, 25 mm) using reusable polypropylene syringe filter holders (Millipore Swinnex, 25 mm). Samples and reference standards for XAS were sealed between 2 layers of Kapton tape and stored in an anaerobic chamber. Analysis was conducted at the Pacific Northwest Consortium X-ray Science Division (PNC/XSD) facility bending magnet beamline (20-BM) at the Advanced Photon Source (SI Section S4). Data reduction and analysis was performed using the Athena XAS data analysis software program.[31]

Aqueous Phase Analysis. Samples were filtered through a 0.2-μm nylon syringe filter, and subsamples (100 μL) were analyzed immediately for Fe(II) and total Fe concentrations via the Ferrozine method.[32,33] A 1.0-mL aliquot of the filtrate was acidified immediately to a final concentration of 1% HCl and stored at −20 °C for As(III) and As(V) speciation determination using a modified molybdenum method (SI Section S5).[34−36] The remaining filtrate was diluted and acidified, and aqueous elemental concentrations were determined using inductively coupled plasma optical emission spectroscopy (ICP-OES).

Thermodynamic Modeling. Eh, pH, and measured aqueous concentrations of Fe(II), Fe(III), Pb, and As were used to calculate equilibrium aqueous activities and saturation indices for the control and inoculated dissolution experiments using The Geochemist's Workbench Software Package (GWB, version 7.06) and the LLNL thermodynamic database.[37]

Calculation of $\Delta G°_f$ for Pb–As Jarosite, $\Delta G°_{rxn}$, and ΔG for the Redox Couples. The Gibbs free energy of formation ($\Delta G°_f$) is not available for beaudantite (i.e., Pb–As jarosite).[8,11] Therefore, the $\Delta G°_f$ of Pb–As jarosite was calculated using the method developed by Gaboreau and Viellard, based on an empirical parameter: $\Delta_G O^{=} M^{z+}{}_{(c)}$, which characterizes the oxygen affinity of structural cations (M^{z+}) within the jarosite structure.[38,39] To examine the thermodynamic constraints on Fe, As, and S reduction in Pb–As jarosite in inoculated samples, the standard state Gibbs free energy of reactions ($\Delta G°_{rxn}$) for aqueous and structural AsO_4^{3-}, Fe and sulfate reduction coupled to lactate oxidation were calculated from compiled values of Gibbs free energy of formation ($\Delta G°_f$) for relevant reaction constituents (SI Table S1). To determine the thermodynamic driving force (i.e., ΔG) for aqueous As(V), aqueous Fe(III), and structural Fe(III) reduction, experimental concentrations of aqueous As(III), As(V), and Fe(II) were used and concentrations of lactate, acetate, and HCO_3^- were estimated assuming a 4:1 and 2:1 stoichiometry for Fe(II) and As(III) production. Due to the high background S concentrations contributed by the PIPES buffer (2 mM) during acidification for ICP-OES preparation, S concentrations were estimated assuming an Fe(II):S ratio of 1:1.7. Low concentrations of Fe(III) and Pb were chosen (10^{-6} μM Fe and 1 μM Pb) to account for nondetection in experimental samples. Minimal media component concentrations, and measured and estimated aqueous concentrations of Fe(II), Fe(III), As(V), As(III), and SO_4^{2-} were used to calculate equilibrium aqueous activities using the extended form of the Debye–Huckel equation using the React program within The Geochemist's Workbench Software Package (GWB, version 7.06) (SI Table S2).[37] The estimated $\Delta G°_f$ for Pb–As jarosite and species activities were incorporated in the Lewis equation and the nonstandard state Gibbs free energy of reaction (ΔG) was determined at 298 K and 1 atm pressure.

RESULTS AND DISCUSSION

Control Pb–As Jarosite Samples. In control Pb–As jarosite samples (i.e., no bacteria), Pb remained below ICP-OES detection limits (10.5 μM) and As release was minimal, reaching a plateau at 20 μM at 72 h (Figure 1). Aqueous As speciation analysis confirmed the oxidation state of As as As(V) (Figure 1). Fe(II) was undetected in control samples and total aqueous Fe concentrations (ICP-OES) were low and remained between 10 and 19 μM throughout the experiment (data not shown). Given the poor solubility of Fe(III) (10^{-9} μM) under circumneutral conditions, the aqueous Fe measured is more likely the result of Fe oxide colloids precipitated during Pb–As dissolution which passed through filtration (<0.2 μM), and subsequently dissolved during acidification for ICP-OES sample preparation.[40] XANES analysis of the control bulk solid phase (i.e., no bacteria) over time at the Fe–K and As–K edge confirmed that Fe and As were present as Fe(III) and As(V) (SI Figure S1). The pH remained buffered at 7.3 throughout the experiment while the redox potential (Eh) reached a plateau of 227–243 RmV between 168 and 336 h (Figure 1). X-ray diffraction patterns collected on the solid phase at 72 and 336 h were similar to the unreacted Pb–As jarosite and showed no extra peaks (SI Figure S2). However, TEM images of the control Pb–As jarosite sample at 336 h show secondary precipitation and EDS analyses of precipitates showed enrichment of Fe (25 wt %), O (39 wt %), As (19 wt %), and Pb (15 wt %) (SI Figures S3 and S4, SI Table S4).

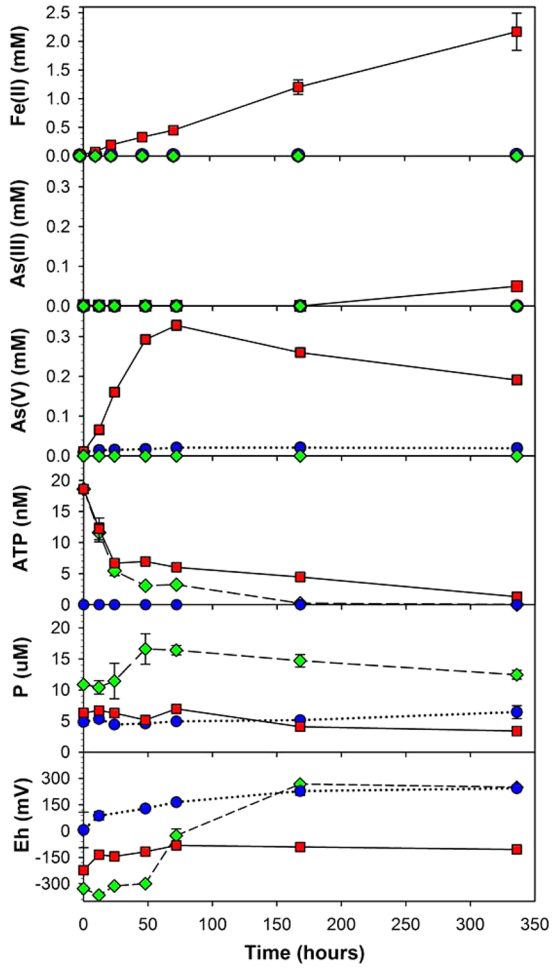

Figure 1. Fe(II), As(III), As(V), ATP, P concentrations and Eh in inoculated minimal media control (i.e., no Pb-As jarosite) (♦, green), Pb–As jarosite control (no bacteria) (●, blue), and inoculated Pb–As jarosite (■, red) samples over time. Error bars represent standard error (n = 3).

Mineral saturation indices (log Q/K) calculated by The Geochemist's Workbench (GWB) predicted the formation of hematite > schwertmannite > goethite > ferrihydrite and undersaturation (log Q/K < 0) of anglesite (SI Table S3). Hematite was discounted as the potential phase because it is expected to form over longer durations, and schwertmannite was discounted because it typically forms between pH 2.8–4.5.[14,41] Based on TEM analyses, the secondary precipitate is likely to be goethite or ferrihydrite. The association of Pb (16 wt %) with the precipitate and the lack of detectable aqueous Pb suggests either surface complexation with $Fe(OH)_3$ or precipitation of another Pb phase such as anglesite ($PbSO_4$).[7] Similarly, the association of As with the precipitate may also be the result of complexation of AsO_4^{3-} with the Fe-oxyhydroxide surface through the formation of inner-sphere bidentate binuclear corner and edge-sharing complexes or coprecipitation.[42,43]

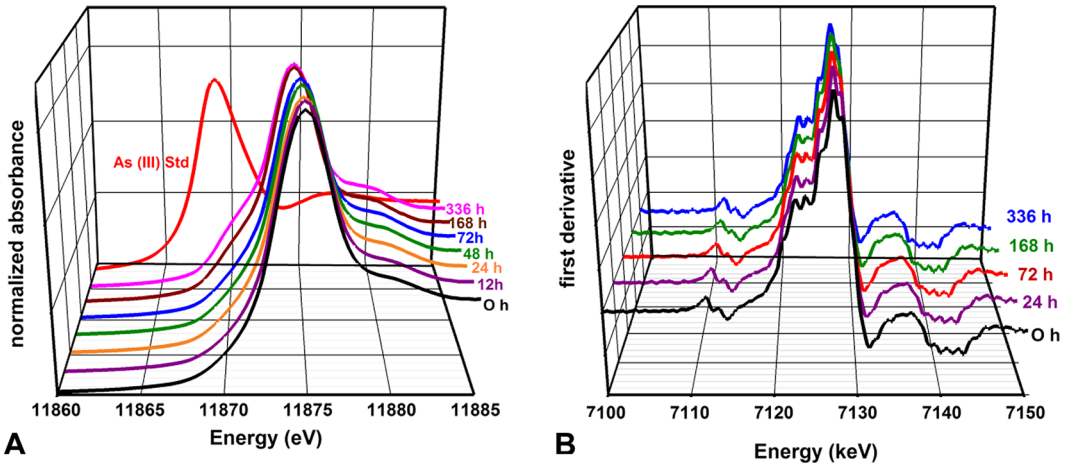

Figure 2. Normalized (A) absorbance As K-edge and (B) first derivative Fe K-edge XANES spectra for inoculated Pb–As jarosite samples over time.

Table 1. Standard State Gibbs Free Energy for Pertinent Redox Reactions

	reactions considered	ΔG°_{rxn} (kJ/mol)
	iron reduction	
1	1.40 $(H_3O)_{0.68}Pb_{0.32}Fe_{2.86}(SO_4)_{1.69}(AsO_4)_{0.31}(OH)_{5.59}(H_2O)_{0.41}$ + $C_3H_5O_3^-$ + 2.31 H^+ → CH_3COO^- + HCO_3^- + 0.45 Pb^{2+} + 4.00 Fe^{2+} + 0.43 $HAsO_4^{2-}$ + 2.37 SO_4^{2-} + 7.35 H_2O	−377.04
2	4.00 $Fe(OH)_2^+$ + $C_3H_5O_3^-$ + 3 H^+ → 4.00 Fe^{2+} + CH_3COO^- + HCO_3^- + 6.00 H_2O	−480.68
	arsenic reduction	
3	2 $HAsO_4^{2-}$ + $C_3H_5O_3^-$ + 3 H^+ → 2 H_3AsO_3 + CH_3COO^- + HCO_3^-	−296.20
4	6.45 $(H_3O)_{0.68}Pb_{0.32}Fe_{2.86}(SO_4)_{1.69}(AsO_4)_{0.31}(OH)_{5.59}(H_2O)_{0.41}$ + $C_3H_5O_3^-$ → CH_3COO^- + HCO_3^- + 0.23 H^+ + 2.065 Pb^{2+} + 18.45 $Fe(OH)_2^+$ + 2.00 H_3AsO_3 + 10.90 SO_4^{2-} + 6.19 H_2O +181.92	
	sulfate reduction	
5	0.30 $(H_3O)_{0.68}Pb_{0.32}Fe_{2.86}(SO_4)_{1.69}(AsO_4)_{0.31}(OH)_{5.59}(H_2O)_{0.41}$ + $C_3H_5O_3^-$ → CH_3COO^- + HCO_3^- + 0.41 H^+ + 0.09 Pb^{2+} + 0.85 $Fe(OH)_2^+$ + 0.09 $HAsO_4^{2-}$ + 0.5 HS^- + 0.28 H_2O	−96.66
6	0.5 SO_4^{2-} + $C_3H_5O_3^-$ →0.5 HS^- + CH_3COO^- + HCO_3^- + 0.5 H^+	−65.39

Inoculated Samples. Inoculated Pb–As jarosite samples remained buffered at pH 7.3 throughout the experiment. The redox potential (Eh) increased from −223 mV at time 0 to −134 mV by 24 h and remained between −134 and −81 RmV for the rest of the experiment (Figure 1). Similarly to the control Pb–As jarosite samples without bacteria, Pb remained below detection limits (DL = 10 μM) in all samples. Higher concentrations of aqueous As(V) were released from inoculated samples than in the controls at a rate of 4.6 ± 2.2 μM·h^{-1} (r^2 = 0.948) until 72 h where concentrations reached a maximum of 0.33 ± 0.012 mM (Figure 1). After 72 h, As(V) concentrations decreased at a rate of 0.71 ± 0.41 μM·h^{-1} to a final concentration of 0.19 ± 0.013 μM. During the last sampling interval, 0.050 ± 0.00 15 μM of As(III) was detected (DL = 6.3 μM) (Figure 1). It is possible that aqueous As(V) reduction/release may have occurred earlier but the 12.5× dilution of arsenic speciation samples would have precluded As(III) detection.

EXAFS modeling of the unreacted (original) Pb–As jarosite suggests that it contains Fe(III) in octahedral coordination with O, and As(V) in tetrahedral coordination with O substituting for S in the structure (SI Section S6). A comparison of the normalized absorption As K-edge spectra of inoculated solid phase samples over time shows a shift (ca. 1 eV) to the lower energy As(III) edge at 168 and 336 h (Figure 2 and SI Figure S1). The proportion of As(III) to As(V) in the solid phase samples in the inoculated Pb–As jarosite over time was determined by linear least-squares combination fitting of XANES spectra using the spectra of sodium meta-arsenite, orpiment, realgar, and the pure unreacted Pb–As jarosite. Least-squares fitting of earlier samples showed 100% As(V), and fitting of the inoculated sample at 168 and 336 h showed 14.7% As(III) (as sodium meta-arsenite)/85.3% As(V) (R factor: 0.0082) and 20.4% As(III) (as sodium meta-arsenite)/79.6% As(V) (R factor: 0.0096), respectively.

In contrast to the As(V) reduction lag time, Fe(III) reduction was observed in the aqueous phase within the first sampling period (0 h) and likely occurred in the time between inoculation and ferrozine analysis (ca. 1 h) (Figure 1). Fe(II) concentrations increased throughout the experiment at a rate of 7.03 ± 0.46 μM·h^{-1} (r^2 = 0.997) to a maximum of 2.2 ± 0.32 mM at the termination of the experiment. Therefore, Fe(III) and As(V) reduction occurred simultaneously from at least 168 h onward (Figures 1 and 2 and SI Figure S1). The normalized first derivative Fe K-edge XANES spectra of the reacted solid phase does not show a shift to the lower Fe(II) energy edge over time thereby suggesting that the majority of Fe(II) (at least 95%) is associated with the aqueous phase (Figure 2). By combining aqueous concentrations with XANES fitting at 336 h, As(III) and Fe(II) represented 23% and 12%, respectively, of the total As and Fe available from the original Pb–As jarosite. An initial ∼1:1 release of Fe(II):As(V) for the first 72 h of the experiment is not surprising because while Pb–As jarosite has a Fe:As molar ratio of 9:1, structurally the Fe octahedra is sterically remote (SI Section S6, SI Figure S11) and less susceptible to dissolution than the sulfate and arsenate tetrahedral sites.[7] Smith et al. showed that during the dissolution of K jarosite, the K and SO_4^{2-} remained exposed

at the surface and the Fe octahedra rotated into the bulk structure.[44] Therefore, the similar release of Fe(II) and As(V) at the beginning of the experiment may be due to the increased surface exposure of AsO_4^{3-} relative to Fe. However, this effect would become less pronounced over time as more Pb^{2+}, AsO_4^{3-}, and SO_4^{2-} are liberated and the Fe octahedra are exposed. Therefore, to elucidate the potential underlying mechanisms behind the simultaneous reduction of Fe and As, the thermodynamic constraints of each redox couple in the aqueous and solid phase were considered.

Standard versus Reaction State Thermodynamic Favorability. Pb−As jarosite presents an interesting opportunity for metal and metalloid reducing bacteria because it contains three potential terminal electron acceptors (TEA) from which to derive energy: Fe, As, and S. Therefore, to determine the relative thermodynamic favorability of TEAs in the Pb−As jarosite, the constraints of both aqueous and structural Fe, As, and S on standard state (ΔG°_f) versus reaction state (ΔG) Gibbs free energy were considered. Calculations of ΔG°_f under standard state conditions predicted aqueous $Fe(OH)_2^+$ reduction as the most favorable reaction on a per mole of lactate basis followed by structural Fe, aqueous $HAsO_4^{2-}$, structural S, and aqueous SO_4^{2-} (Table 1). Moreover, with a ΔG°_{rxn} = +181.92 kJ/mol, structural As(V) reduction is not favorable, which may partly account for the aqueous As(V) reduction observed in this study. The contribution of the concentration gradients established by the reactants and products over time under nonstandard conditions (Q) were considered and the ΔG under nonstandard state was calculated.[25] The reaction quotient (Q) at each time interval was calculated and incorporated into the Lewis equation for ΔG for the 3 most likely reduction reactions predicted to occur: $Fe(OH)_2^+$ (eq 1), structural Fe (eq 2), and aqueous $HAsO_4^{2-}$ (eq 3):

$$\Delta G_r = \Delta G_r^\circ + 2.3RT\log((\{CH_3COO^-\}\{HCO_3^-\}\{Fe^{2+}\}^4)/(\{Fe(OH)_2^+\}^4\{C_3H_5O_3^-\}\{H^+\}^3)) \quad (1)$$

$$\Delta G_r = \Delta G_r^\circ + 2.3RT\log((\{CH_3COO^-\}\text{-}\{HCO_3^-\}\text{-}\{Pb^{2+}\}^{0.45}\text{-}\{Fe^{2+}\}^4\text{-}\{HAsO_4^{2-}\}^{0.43}\text{-}\{SO_4^{2-}\}^{2.37})/(\{C_3H_5O_3^-\}\text{-}\{H^+\}^{2.31})) \quad (2)$$

$$\Delta G_r = \Delta G_r^\circ + 2.3RT\log((\{CH_3COO^-\}\{HCO_3^-\}\{H_3AsO_3\}^2)/(\{HAsO_4^{2-}\}^2\{C_3H_5O_3^-\}\{H^+\}^3)) \quad (3)$$

Calculations of ΔG at each time interval for the redox couples show that the reduction of structural Fe(III) within the Pb−As jarosite (eq 2) is much more thermodynamically favorable over time as compared to aqueous Fe(III) and As(V) reduction (Figure 3). In this study, we did not experimentally determine if *S. putrefaciens* reduced structural or aqueous Fe. However, in order for aqueous Fe(III) reduction to proceed, rapid abiotic dissolution would need to occur to continuously provide aqueous Fe(III) activities sufficient for continued energy gain by *S. putrefaciens*.[25] Based on the minimal dissolution of the Pb−As jarosite control samples (i.e., no bacteria), it is unlikely that abiotic dissolution would provide enough aqueous Fe(III) for continued reduction. Therefore, the thermodynamic favorability of structural Fe reduction coupled with the higher Fe:As (~9:1) in the structure leads us to hypothesize that additional factors are driving As(V) reduction.

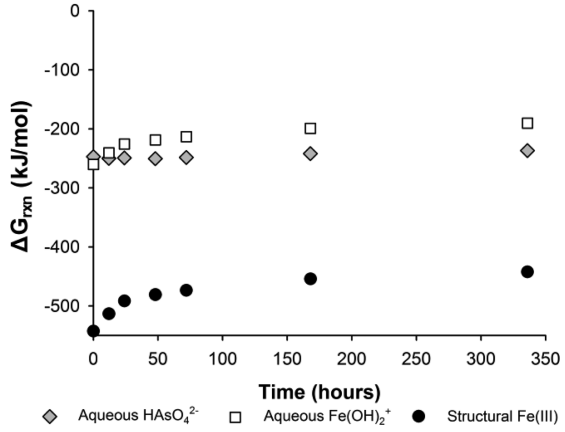

Figure 3. ΔG_{rxn} calculated for aqueous As(V), structural and aqueous Fe(III) reduction coupled to lactate oxidation based on experimental conditions over time.

Microbial As(V) Reduction Mechanism. The increased concentrations of As(V) released from the Pb−As jarosite over time may be a potential trigger for the As detoxification mechanism (*arr* system). Saltikov et al. demonstrated a correlation between As(V) concentrations and *ars*/*arr* expression in an As-tolerant Shewanella species (*Shewanella* sp. ANA-3) whereby respiration occurred at low concentrations (100 nM) earlier in cell growth and detoxification at higher concentrations (~100 μM) during stationary phase.[2] Jiang et al. showed 93.7 and 100% protein sequence similarities in *S. putrefaciens* CN32 to the proteins encoded by the *arr*−*ars* operon from *Shewanella sp.* strain ANA-3 thereby providing evidence for both As reduction pathways in *S. putrefaciens* CN32.[45] Therefore, the As(V) reduction time lag in the inoculated Pb−As jarosite samples may be the result of detoxification (*ars*) induced by high aqueous As(V) concentrations (328 μM). Alternatively, the accumulation of precipitates or metabolites may have diminished the thermodynamic favorability of Fe(III) reduction and triggered simultaneous respiratory As reduction (*arr*). Therefore, the reduction mechanism is unclear and in the absence of gene expression data, the As(V) reduction process cannot be confirmed and requires further elucidation.

ATP Analyses. An ATP-based cell viability assay was used to evaluate ATP concentrations over time to examine the potential toxicity of As and Pb on *S. putrefaciens* CN32 (Figure 1). Statistical analyses (t test) of the variation in initial and ATP concentrations at each time interval between inoculated minimal media with or without Pb−As jarosite showed significantly higher ATP in samples containing Pb−As jarosite at 48, 72, and 168 h where p = 0.0039, 0.0033, and 0.0007, respectively. Increased ATP in the inoculated Pb−As jarosite samples may be attributed to the ATP generated during normal Fe reduction, however, *S. putrefaciens* CN32 previously demonstrated reduced ATP concentrations as compared to control samples when exposed to potentially toxic metals such as Pb.[21] As proposed by Chow et al., the higher ATP concentrations in the Pb−As jarosite samples may be the result of increased Fe reduction triggered by *S. putrefaciens* to compensate for the ATP lost during hydrolysis to maintain active transport As(III) out of the cell.[46]

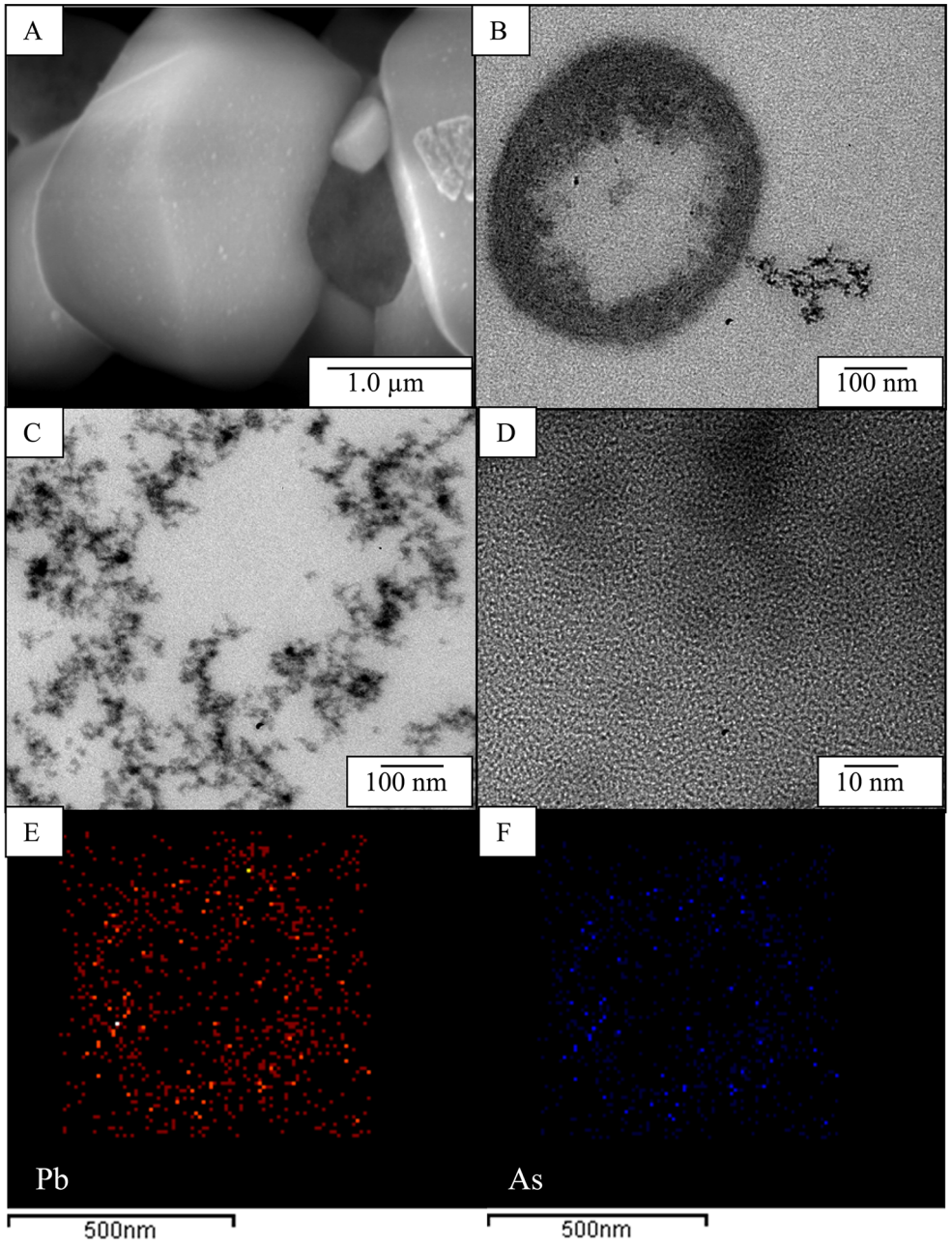

Figure 4. (A) SE-SEM image of secondary mineral precipitates associated with inoculated Pb–As jarosite at 336 h, and TEM images of (B) *S. putrefaciens* associated with secondary minerals at 72 h; (C) secondary precipitates at 336 h; and (D) corresponding HR-TEM image of the precipitate in C; (E) and (F) TEM-EDS Pb and As maps of a cross sectioned *S. putrefaciens* cell (from B) at 336 h. Maps of P, Fe, and O of the same cell are found in SI Figure S10.

In a previous study, the reductive dissolution of Pb jarosite by *S. putrefaciens* under similar conditions showed minimal Fe(III) reduction with a maximum of ~200 μM Fe(II) versus the 2166 μM observed in the current study.[21] Therefore, the enhanced Fe(III) reduction (10×) observed in this study may be a response by *S. putrefaciens* to high As(V) concentrations to maintain the ATP required for active As(III) efflux.

Solid Phase Characterization of Inoculated Pb–As Jarosite Samples. Bulk X-ray diffraction patterns collected on inoculated samples over time were similar to the original unreacted jarosite and did not show any new peaks (SI Figure S2). SEM images taken over time do not reveal significant dissolution (SI Figure S5). However, high-resolution SEM images of inoculated Pb–As jarosite at 336 h reveal a surface coating of secondary precipitates (Figure 4A). EDS spectra collected at randomly selected areas on the bulk jarosite at 0, 168, and 336 h demonstrated enrichment of Pb (from 16 to 20%) (SI Table S5). By contrast, As increases from 1.4 wt % at time 0 to 4.7 wt % at 168 h, followed by a decrease to 1.6 wt % by 336 h (SI Table S5), the latter of which is also coincident with the increase of aqueous As(III) (Figure 1). TEM images of a *S. putrefaciens* cell at 72 h (Figure 4B) show precipitates in close proximity to the cell. An elemental map of precipitates shows relative enrichment of Fe, P, and O (SI Figure S6). Furthermore, TEM-EDS analysis of several precipitates shows enrichment of Fe (24 wt %), P (3 wt %), O (64 wt %), and sometimes As (8.5 wt %) (SI Figure S7), while TEM images also reveal an amorphous structure (Figure 4C and D).

However, it is also possible that the P associated with the precipitates or cells is a reflection of As release and P uptake by the precipitates during immersion in the phosphate buffer during TEM sample preparation. ICP-OES analysis of the minimal media (i.e., no Pb−As jarosite or bacteria) at 0 and 336 h shows a background P concentration of ∼8 μM. Inoculated minimal media without Pb−As jarosite contributed to an increase in P over background concentrations likely related to cell lysis (Figure 1). Release of P in these samples showed an increase in P from 11 μM at time 0 to 16 μM followed by a decrease to 12 μM by 336 h. Pb−As samples inoculated with *S. putrefaciens* showed a gradual P decline from 6.3 to 3.4 μM at the end of the experiment. Mineral saturation indices (log Q/K) predict the formation of vivianite ($Fe_3(PO_4)_2{\cdot}H_2O$) and siderite ($FeCO_3$) and the under saturation of $Fe(OH)_2$ and cerrusite ($PbCO_3$) (SI Table S3).

Fate of As and Pb. While vivianite has been proposed as an As sink in previous studies, the low concentrations of P (∼ 12 μM) in our samples make it unlikely that vivianite is the primary sink for As sorption and retention in this experiment. Therefore, it is more plausible that arsenite and P were sorbing to the siderite predicted to form. The identification of siderite could not be determined using TEM-EDS due to the background contribution of carbon from the carbon-coated Formvar sample grid. The observed release of aqueous As(III) at 336 h may be due to increasing As(III) reduction and the lack of sorption sites due to minimal secondary precipitation. Tufano et al. showed As(III) retention during early Fe reduction from ferrihydrite-coated sands presorbed with As(III) using *S. putrefaciens* CN32, but over time the cessation of phase transformations resulted in the release of aqueous As(III).[47]

Interestingly, intracellular Pb accumulation was not observed in this study, yet was previously demonstrated during the reductive dissolution of Pb jarosite by the same freezer stock of *S. putrefaciens* CN32.[21] Therefore, it is possible that the energy derived from ATP efflux was sufficient to remove Pb from the cell. Elemental maps of cross sections of *S. putrefaciens* cells show relative increased localization of As and Pb at the cell wall from time 0 to 336 h (SI Figures S8 and S9). The enrichment of As at the cell wall likely represents As(V) sorption prior to uptake, reduction, and efflux of As(III) from the cell. The localization of Pb at the cell wall is likely due to the formation of adsorption complexes with carboxyl and phosphoryl functional groups commonly reported at circumneutral conditions.[21,48,49]

Environmental Implications. This study demonstrates the simultaneous reduction of Fe(III) and As(V) during the microbial dissolution of synthetic Pb−As jarosite. Additionally, aqueous Pb release was not observed in both the control and inoculated samples. Despite the low molar content of As in the original Pb−As jarosite, high concentrations of aqueous As(V) were released in samples containing *S. putrefaciens* as compared to the abiotic control. Therefore, depending on the microbial communities present, Pb−As jarosite does not represent a suitable candidate for arsenical waste storage under anaerobic circumneutral conditions and As and Pb release may become enhanced in the presence of bacteria. However, the effects of temperature, flow, competing microbial communities, natural organic matter, suspension density, or removal of As onto potentially coexisting Fe-oxides on the reduction kinetics and fate of As were not considered, leaving opportunity for future refinement.[7] Finally, future studies should assess the reductive dissolution of Pb−As jarosite using arsenate- and sulfate-reducing bacteria and microbial consortia collected from mine waste repositories to improve our understanding of Pb−As jarosite solubility.

■ ASSOCIATED CONTENT

Supporting Information

Additional details including preparation of *S. putrefaciens*, ATP, TEM, SEM, XAS, and XRD analysis/results, As speciation method, thermodynamic data, geochemical modeling parameters/results. This material is available free of charge via the Internet at http://pubs.acs.org.

■ AUTHOR INFORMATION

Corresponding Author

*E-mail: christina.smeaton@uwaterloo.ca or christinasmeaton@gmail.com; phone: (519) 888-4567 ext. 32820; fax: (519) 746-7484.

Present Addresses

[#]Department of Microbiology, University of Tennessee, Knoxville, Tennessee, 37996, United States.

[¶]Nanochemistry Research Institute, Department of Chemistry, Curtin University, GPO Box U1987, Perth, WA 6845, Australia.

[▼]University of Utrecht, Debye Institute, Department of Inorganic Chemistry and Catalysis, Sorbonnelaan 16, 3584 CA Utrecht, The Netherlands.

[○]Ecohydrology Research Group, Department of Earth and Environmental Sciences, University of Waterloo, Waterloo, Ontario N2L 3G1, Canada.

Notes

The authors declare no competing financial interest.

■ ACKNOWLEDGMENTS

We thank NSERC for financial support. We also thank Megan Goetz, Candace McCort, Michael Dufour, Matt Smith, and J.C. Barrette for laboratory assistance. We also thank Marcia Reid and Andreas Korinek at McMaster for TEM sample preparation and analysis assistance. We thank Dale Brewe, Robert Gordon, Steve Heald, and Mike Pape for their assistance at the APS. PNC/XSD facilities at the Advanced Photon Source, and research at these facilities, are supported by the US Department of Energy - Basic Energy Sciences, a Major Resources Support grant from NSERC, the University of Washington, the Canadian Light Source and the Advanced Photon Source. Use of the Advanced Photon Source, an Office of Science User Facility operated for the U.S. Department of Energy (DOE) Office of Science by Argonne National Laboratory, was supported by the U.S. DOE under Contract No. DE-AC02-06CH11357.

■ REFERENCES

(1) Nordstrom, D. K. Worldwide occurrences of arsenic in ground water. *Science* **2002**, *296* (5576), 2143.

(2) Saltikov, C. W.; Wildman, R. A., Jr.; Newman, D. K. Expression dynamics of arsenic respiration and detoxification in Shewanella sp. strain ANA-3. *J. Bacteriol.* **2005**, *187* (21), 7390.

(3) Islam, F. S.; Gault, A. G.; Boothman, C.; Polya, D. A.; Charnock, J. M.; Chatterjee, D.; Lloyd, J. R. Role of metal-reducing bacteria in arsenic release from Bengal delta sediments. *Nature* **2004**, *430* (6995), 68−71.

(4) Kocar, B. D.; Polizzotto, M. L.; Benner, S. G.; Ying, S. C.; Ung, M.; Ouch, K.; Samreth, S.; Suy, B.; Phan, K.; Sampson, M. Integrated biogeochemical and hydrologic processes driving arsenic release from

shallow sediments to groundwaters of the Mekong delta. *Appl. Geochem.* **2008**, *23* (11), 3059−3071.
(5) Nickson, R.; McArthur, J.; Burgess, W.; Ravenscroft, P.; Ahmed, K. Arsenic poisoning of Bangladesh groundwater. *Nature* **1988**, *395*, 338.
(6) Savage, K. S.; Bird, D. K.; O'Day, P. A. Arsenic speciation in synthetic jarosite. *Chem. Geol.* **2005**, *215* (1), 473−498.
(7) Smith, A. M. L.; Dubbin, W. E.; Wright, K.; Hudson-Edwards, K. A. Dissolution of lead- and lead-arsenic-jarosites at pH 2 and 8 and 20 degrees C: Insights from batch experiments. *Chem. Geol.* **2006**, *229* (4), 344−361.
(8) Frost, R. L.; Palmer, S. J.; Spratt, H. J.; Martens, W. N. The molecular structure of the mineral beudantite $PbFe_3(AsO_4,SO_4)_2(OH)_6$ - Implications for arsenic accumulation and removal. *J. Mol. Struct.* **2011**, *988* (1−3), 52−58.
(9) Paktunc, D.; Dutrizac, J. E. Characterization of arsenate-for-sulfate substitution in synthetic jarosite using X-ray diffraction and X-ray absorption spectroscopy. *Can. Mineral.* **2003**, *41* (4), 905−919.
(10) Chiang, K. Y.; Lin, K. C.; Lin, S. C.; Chang, T. K.; Wang, M. K. Arsenic and lead (beudantite) contamination of agricultural rice soils in the Guandu Plain of northern Taiwan. *J. Hazard. Mater.* **2010**, *181* (1), 1066−1071.
(11) Szymanski, J. T. The crystal structure of beudantite, $Pb(Fe,Al)_3[(As,S)O_4]_2(OH)_6$. *Can. Mineral.* **1988**, *26* (4), 923−932.
(12) Dutrizac, J. E. Jarosite-type compounds and their application in the metallurgical industry. *J. Metals* **1982**, *35* (12), A70−A70.
(13) Dutrizac, J. E.; Jambor, J. L. Jarosites and their application in hydrometallurgy. In *Sulfate Minerals - Crystallography, Geochemistry and Environmental Significance*; Mineralogical Society of America, 2000; Vol. *40*, pp 405−452.
(14) Bigham, J.; Schwertmann, U.; Traina, S.; Winland, R.; Wolf, M. Schwertmannite and the chemical modeling of iron in acid sulfate waters. *Geochim. Cosmochim. Acta* **1996**, *60* (12), 2111−2121.
(15) Bigham, J.; Nordstrom, D. K. Iron and aluminum hydroxysulfates from acid sulfate waters. *Rev. Mineral. Geochem.* **2000**, *40* (1), 351.
(16) Paktunc, D.; Dutrizac, J. E. Characterization of arsenate-for-sulfate substitution in synthetic jarosite using X-ray diffraction and X-ray absorption spectroscopy. *Can. Mineral.* **2003**, *41* (4), 905−919.
(17) Al, T. A.; Blowes, D. W.; Jambor, J. L.; Scott, J. D. The geochemistry of mine-waste pore-water affected by the combined disposal of natrojarosite and base-metal sulfide tailings at Kidd Creek, Timmins, Ontario. *Can. Geotech. J.* **1994**, *31* (4), 502−512.
(18) Sunyer, A.; Vinals, J. Arsenate substitution in natroalunite: A potential medium for arsenic immobilization. Part 1: Synthesis and compositions. *Hydrometallurgy* **2011**, *109* (1−2), 54−64.
(19) Kolitsch, U.; Pring, A. Crystal chemistry of the crandallite, beudantite and alunite groups: a review and evaluation of the suitability as storage materials for toxic metals. *J. Mineral. Pet. Sci.* **2001**, *96* (2), 67−78.
(20) Coggon, M.; Becerra, C. A.; Nusslein, K.; Miller, K.; Yuretich, R.; Ergas, S. J. Bioavailability of jarosite for stimulating acid mine drainage attenuation. *Geochim. Cosmochim. Acta* **2012**, *78*, 65−76.
(21) Smeaton, C. M.; Fryer, B. J.; Weisener, C. G. Intracellular precipitation of Pb by *Shewanella putrefaciens* CN32 during the reductive dissolution of Pb-Jarosite. *Environ. Sci. Technol.* **2009**, *43* (21), 8091−8096.
(22) Weisener, C. G.; Babechuk, M. G.; Fryer, B. J.; Maunder, C. Microbial dissolution of silver jarosite: Examining its trace metal behaviour in reduced environments. *Geomicrobiol. J.* **2008**, *25* (7−8), 415−424.
(23) Burnol, A.; Garrido, F.; Baranger, P.; Joulian, C.; Dictor, M. C.; Bodenan, F.; Morin, G.; Charlet, L. Decoupling of arsenic and iron release from ferrihydrite suspension under reducing conditions: a biogeochemical model. *Geochem. Trans.* **2007**, *8*, 12.
(24) Campbell, K. M.; Malasarn, D.; Saltikov, C. W.; Newman, D. K.; Hering, J. G. Simultaneous microbial reduction of iron (III) and arsenic (V) in suspensions of hydrous ferric oxide. *Environ. Sci. Technol.* **2006**, *40* (19), 5950−5955.
(25) Kocar, B. D.; Fendorf, S. Thermodynamic constraints on reductive reactions influencing the biogeochemistry of arsenic in soils and sediments. *Environ. Sci. Technol.* **2009**, *43* (13), 4871−4877.
(26) Tufano, K. J.; Fendorf, S. Confounding impacts of iron reduction on arsenic retention. *Environ. Sci. Technol.* **2008**, *42* (13), 4777−4783.
(27) Huang, J. H.; Elzinga, E. J.; Brechbuehl, Y.; Voegelin, A.; Kretzschmar, R. Impacts of *Shewanella putrefaciens* strain CN-32 cells and extracellular polymeric substances on the sorption of As (V) and As (III) on Fe (III)-(hydr) oxides. *Environ. Sci. Technol.* **2011**, *45* (7), 2804−2810.
(28) Huang, J. H.; Voegelin, A.; Pombo, S. A.; Lazzaro, A.; Zeyer, J.; Kretzschmar, R. Influence of arsenate adsorption to ferrihydrite, goethite, and boehmite on the kinetics of arsenate reduction by *Shewanella putrefaciens* strain CN-32. *Environ. Sci. Technol.* **2011**, *45* (18), 7701−7709.
(29) Kocar, B. D.; Herbel, M. J.; Tufano, K. J.; Fendorf, S. Contrasting effects of dissimilatory iron (III) and arsenic (V) reduction on arsenic retention and transport. *Environ. Sci. Technol.* **2006**, *40* (21), 6715−6721.
(30) Hammes, F.; Goldschmidt, F.; Vital, M.; Wang, Y. Y.; Egli, T. Measurement and interpretation of microbial adenosine tri-phosphate (ATP) in aquatic environments. *Water Res.* **2010**, *44* (13), 3915−3923.
(31) Ravel, B.; Newville, M. Athena, Arthemis, Hephaestus: data analysis for X-ray absorption spectroscopy using IFEFFIT. *J. Synchrotron Radiat.* **2005**, *12* (4), 537−541.
(32) Stookey, L. L. Ferrozine - A new spectrophotometric reagent for iron. *Anal. Chem.* **1970**, *42* (7), 779−781.
(33) Viollier, E.; Inglett, P. W.; Hunter, K.; Roychoudhury, A. N.; Van Cappellen, P. The ferrozine method revisited: Fe(II)/Fe(III) determination in natural waters. *Appl. Geochem.* **2000**, *15* (6), 785−790.
(34) Dhar, R. K.; Zheng, Y.; Rubenstone, J.; van Geen, A. A rapid colorimetric method for measuring arsenic concentrations in groundwater. *Anal. Chim. Acta* **2004**, *526* (2), 203−209.
(35) Johnson, D. L. Bacterial reduction of arsenate in sea water. *Nature* **1972**, *240*, 44−45.
(36) Cummings, D. E.; Caccavo, F., Jr.; Fendorf, S.; Rosenzweig, R. F. Arsenic mobilization by the dissimilatory Fe (III)-reducing bacterium Shewanella alga BrY. *Environ. Sci. Technol.* **1999**, *33* (5), 723−729.
(37) Bethke, C. *Geochemical and Biogeochemical Reaction Modeling*; Cambridge University Press, 2008.
(38) Vieillard, P. A new method for the prediction of Gibbs free energies of formation of hydrated clay minerals based on the electronegativity scale. *Clays Clay Miner.* **2000**, *48* (4), 459−473.
(39) Gaboreau, S.; Vieillard, P. Prediction of Gibbs free energies of formation of minerals of the alunite supergroup. *Geochim. Cosmochim. Acta* **2004**, *68* (16), 3307−3316.
(40) Schwertmann, U. Solubility and dissolution of iron oxides. *Plant Soil* **1991**, *130* (1), 1−25.
(41) Ford, R. G.; Bertsch, P. M.; Farley, K. J. Changes in transition and heavy metal partitioning during hydrous iron oxide aging. *Environ. Sci. Technol.* **1997**, *31* (7), 2028−2033.
(42) Sherman, D. M.; Randall, S. R. Surface complexation of arsenic (V) to iron (III)(hydr) oxides: structural mechanism from ab initio molecular geometries and EXAFS spectroscopy. *Geochim. Cosmochim. Acta* **2003**, *67* (22), 4223−4230.
(43) Dixit, S.; Hering, J. G. Comparison of arsenic (V) and arsenic (III) sorption onto iron oxide minerals: Implications for arsenic mobility. *Environ. Sci. Technol.* **2003**, *37* (18), 4182−4189.
(44) Smith, A. M. L.; Hudson-Edwards, K. A.; Dubbin, W. E.; Wright, K. Dissolution of jarosite $[KFe_3(SO_4)_2(OH)_6]$ at pH 2 and 8: Insights from batch experiments and computational modelling. *Geochim. Cosmochim. Acta* **2006**, *70* (3), 608−621.
(45) Jiang, S.; Lee, J. H.; Kim, M. G.; Myung, N. V.; Fredrickson, J. K.; Sadowsky, M. J.; Hur, H. G. Biogenic formation of As-S nanotubes

by diverse Shewanella strains. *Appl. Environ. Microbiol.* **2009**, *75* (21), 6896−6899.
(46) Chow, S. S.; Taillefert, M. Effect of arsenic concentration on microbial iron reduction and arsenic speciation in an iron-rich freshwater sediment. *Geochim. Cosmochim. Acta* **2009**, *73* (20), 6008−6021.
(47) Tufano, K. J.; Fendorf, S. Confounding impacts of iron reduction on arsenic retention. *Environ. Sci. Technol.* **2008**, *42* (13), 4777−4783.
(48) Fein, J. B.; Daughney, C. J.; Yee, N.; Davis, T. A. A chemical equilibrium model for metal adsorption onto bacterial surfaces. *Geochim. Cosmochim. Acta* **1997**, *61* (16), 3319−3328.
(49) Templeton, A. S.; Trainor, T. P.; Spormann, A. M.; Newville, M.; Sutton, S. R.; Dohnalkova, A.; Gorby, Y.; Brown, G. E. Sorption versus biomineralization of Pb(II) within *Burkholderia cepacia* biofilms. *Environ. Sci. Technol.* **2003**, *37* (2), 300−307.